Quantitative Analysis of Planar Laser-Induced Fluorescence Measurements in a Hypersonic Boundary Layer

Connor C. McDougall[1], W. Schuyler Hinman[1], Craig T. Johansen[1,*],
Brett F. Bathel[2], Jennifer A. Inman[2], Paul M. Danehy[2]
1: Dept. of Mechanical and Manufacturing Engineering, University of Calgary, Canada
2: Advanced Measurements and Data Systems Branch, NASA Langley Research Center, United States
*Correspondent author: johansen@ucalgary.ca

Keywords: Quantitative PLIF, Nitric oxide, Mole fraction, Heat flux, Pressure, Boundary layer, Hypersonics

ABSTRACT

Several quantitative measurements extracted from nitric oxide (NO) planar laser-induced fluorescence (PLIF) data obtained in a hypersonic boundary layer are reported: (a) off-body NO mole fraction; (b) surface heat flux; and (c) near-wall static temperature. The experimental data was obtained at NASA Langley Research Center's 31 in. Mach 10 air tunnel. NO was seeded into the flow through a spanwise slot on the surface of the 10 degree half-angle wedge model. An ultraviolet planar laser sheet was positioned perpendicular to the wedge surface, downstream of the seeding slot, to excite six fluorescence transitions. A method for extracting the relative NO mole fraction, based on spatial variations of the J″= 0.5 PLIF signal, is presented. Combined with the principle of mass conservation, the absolute NO mole fraction is determined. These measurements were used to assess CFD diffusion modelling, correct previously reported PLIF thermometry results, and develop methods for NO-PLIF heat transfer measurements.

1. Introduction

Understanding hypersonic boundary-layer flows is important in the design of heat shields, high-speed lifting bodies, and engine intakes [1-3]. The aerothermodynamics associated with the boundary layers on these systems, especially in unsteady and turbulent flows, are not well understood [2, 4-6]. While the capability of numerical modeling continues to improve, there is still a need to perform wind-tunnel experiments to observe complex fluid flow features [7]. Specifically, limitations in modelling chemical reactions, non-equilibrium effects, and turbulence are still obstacles for numerical investigations. Physical probes, such as slug calorimeters and Pitot tubes, have been used in hypersonic wind tunnel facilities to measure flow properties [8]. However, physical probes are intrusive, disrupt the natural flow, and often only provide single-point measurements. Most physical probes used in subsonic or low supersonic testing cannot withstand the aerodynamic and heating loads that occur in a hypersonic flow. For these reasons, non-intrusive diagnostics are preferred in hypersonics, but still require further development [9, 10].

Planar laser-induced fluorescence (PLIF), a commonly-used diagnostic in high-speed flows, involves exciting a tracer species to a higher energy state through laser absorption. The subsequent emission of radiation (i.e., fluorescence) is captured by a detector, which can provide detailed visualizations of various fluid mechanics phenomena [11, 12]. The sensitivity of the fluorescence process to thermodynamic properties of the fluid allows for quantitative measurements [13-15]. For example, changes in pressure and temperature can shift the center frequency of the transitions, affect their amplitudes, and broaden the absorbed energy range of the incident radiation [11, 13, 16]. Several spatially-resolved quantitative PLIF experiments have been reported in the literature [13, 16-22]. PLIF, using nitric oxide (NO) as a tracer, has been successful in extracting quantitative measurements, such as temperature, velocity and mole fraction, from high-speed flow [17, 23, 24]. NO-PLIF mole fraction measurements have been performed in hypersonic environments, but require a reference point in the imaging region to obtain quantitative results [19, 24, 25]. Heat flux measurements often depend on an accurate temperature measurement, used in tandem with Fourier's law, to estimate transfer of energy [26]. There has been interest in simultaneously measuring multiple thermophysical properties using one camera system with PLIF imaging techniques [25, 27, 28].

The present study focuses extracting multiple quantitative measurements from a single NO PLIF data set obtained in a hypersonic laminar boundary layer: off-body species mole fraction, surface heat flux, and near-surface static temperature. Boundary layer theory and the Navier-Stokes equations are used to close the problem and extract these additional quantities.

2. Facility & Experimental Setup

NO PLIF was performed on a 10 degree half-angle wedge model in the NASA Langley 31 in. Mach 10 air tunnel facility. The top surface of the wedge was oriented at a 5 degree angle of attack with respect to the oncoming flow. The wedge was held stationary using a sting joining the rear surface of the wedge to the tunnel's side wall. In these flow conditions, an attached oblique shock forms at the leading edge of the wedge. The flow Reynolds number, based on post-shock properties and plate length, was approximately 3.4×10^5, resulting in a laminar boundary layer. At 29.4 mm downstream from the leading edge, a rectangular spanwise slot was used to seed NO into the boundary layer. A detailed summary of this set-up is shown in Figure 1. Flow conditions of the Mach 10 facility are outlined in Table 1.

A Spectra Physics Pro-230 Nd:YAG laser was used to pump a Sirah Cobra Stretch tunable pulsed dye laser with a Sirah Frequency Conversion Unit (FCU). The system operated at 10 Hz with pulse durations of approximately 10 ns. Lenses formed the laser into sheet, which was oriented in the *x*-*y* plane, perpendicular to the surface of the wedge. A 16-bit UV sensitive intensified CCD camera (Princeton Instruments PIMAX) was oriented perpendicular to the laser sheet, pointed across the surface of the wedge. The laser used was tuned to a wavelength of 226.222 nm (44204.37 cm^{-1}) and was scanned spectrally over 75 seconds to 226.232 nm (44202.31 cm^{-1}) during the wind-tunnel test. Three pairs of transitions exist in this spectral range: $Q_1(6.5)$, ${}^{Q}P_{21}(6.5)$, $R_1(0.5)$, ${}^{R}Q_{21}(0.5)$, $Q_2(17.5)$, and ${}^{Q}R_{12}(17.5)$. However, due to overlapping transitions, there are only three distinct excitation lines in the experimental data for each J″ quantum number. The fluorescence transition information, obtained from [29], is outlined in Table 2.

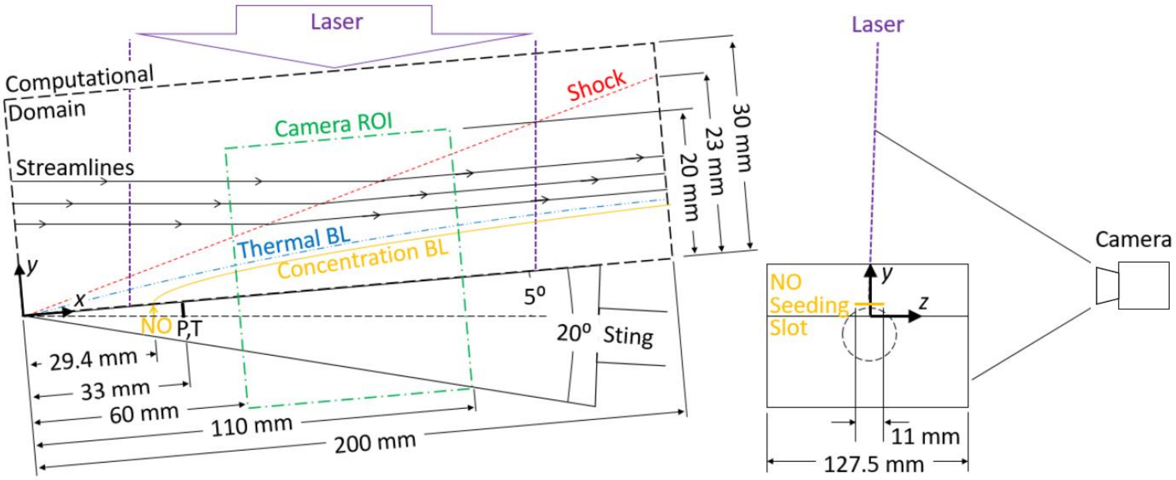

Fig 1. Side-view (left) and front-view (right) schematics of the 10 degree half-angle wedge used in the NASA Langley 31 in. Mach 10 air tunnel. ROI denotes the region of interest.

Table 1. Computed experimental flow conditions (T462 Run 19) used in the NASA Langley 31 in. Mach 10 air tunnel facility

Mach Number	9.7
Free-stream Velocity (m/s)	1407.3
Free-stream Temperature (K)	52.3
Free-stream Pressure (Pa)	68.4
Stagnation Temperature (K)	1000
Stagnation Pressure (MPa)	2.41

Table 2. Table of constants for the targeted transitions in the experiment

Transition	Q_1	$^{Q}P_{21}$	R_1	$^{R}Q_{21}$	Q_2	$^{Q}R_{12}$
Rotational Quantum Number J"	6.5	6.5	0.5	0.5	17.5	17.5
Einstein B12 Coefficient (cm/J)	232.560	70.005	129.551	259.101	282.165	46.954
Center Frequency (/cm)	44202.821	44202.845	44203.578	44202.582	44203.810	44203.886

3. Quantitative Measurements

Three quantitative measurements are presented in this study: NO species mole fraction, surface heat flux, and near-surface static temperature. These quantitative measurements are compared to computational fluid dynamics (CFD) simulations performed by Arisman *et. al.* [30, 31] of the same geometry and flow conditions as reported in the current work. The CFD results are assumed to be an accurate prediction of the flow, due to the laminar flow conditions and simple geometry. Good agreement between the CFD and molecular tagging velocimetry (MTV) [23] and surface pressure measurements obtained in a previous experiment were reported [30]. Thermometry of the current NO-PLIF data, also performed in a previous work [17], showed good agreement with CFD predictions, with the exception of the near-surface temperature. A correction of the near surface temperature based on a heat flux calculation is one of the objectives of the current work. Figure 2 shows the time-averaged experimental NO-PLIF signal map, along with prior CFD results from Arisman *et. al.* [30] that will be used for comparison. The vertical red lines in Figure 2 (a), (c) and (d) indicate the sampling locations (x=60 mm, x=85 mm, and x=110 mm) used for comparison. In these images, the thermal, velocity, and concentration boundary- layer thicknesses are approximately 3 mm. The oblique shock is visible in the pressure and temperature contour maps, roughly at a height between 7 and 12 mm. Since the NO-PLIF signal is limited to the concentration boundary layer, results are only reported up to a height of y = 5 mm. Note that all of the methods outlined below were validated on the numerical data from CFD. For example, the heat flux method, described in Section 3.2, was performed on the off-body temperature profiles from the CFD and then compared directly to the heat flux at the wall boundary. There was a less than 1% difference between these values.

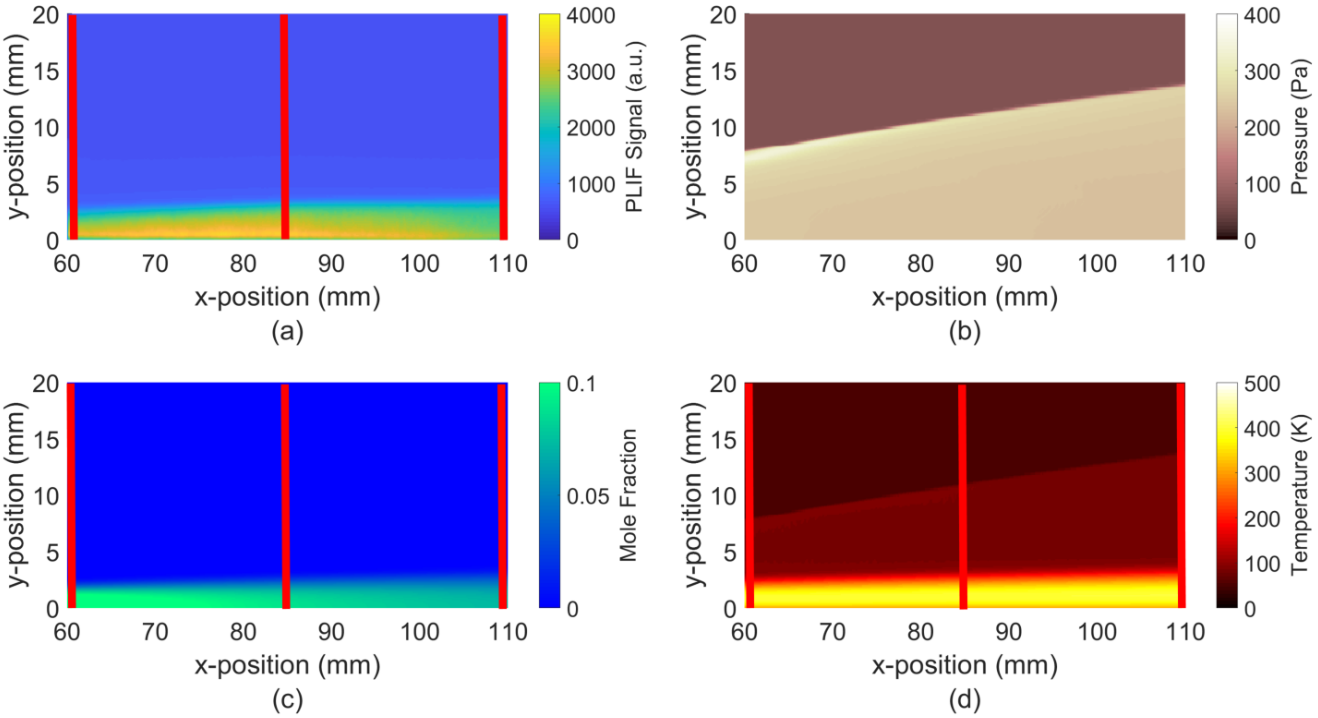

Fig. 2 Contour maps of (a) experimental NO-PLIF signal, (b) CFD pressure, (c) CFD mole fraction, and (d) CFD temperature; red lines indicate sampling locations

3.1 NO Mole Fraction

The mole fraction was determined in a two-step process. First, a relative mole fraction (χ_{rel}) profile was determined using a proportionality relation derived from the well-known LIF equation taken from Palma [13], shown below as Equation 1:

$$\chi_{\mathrm{rel}} = \frac{\chi}{\chi_{\mathrm{wall}}} = \frac{\left(\frac{1}{S_f}\left(\frac{1}{1+s}\right) N_T B_{12} F_B I G \Phi t_{det} V \frac{\Omega}{4\pi}\eta\right)_{\mathrm{wall}}}{\left(\frac{1}{S_f}\left(\frac{1}{1+s}\right) N_T B_{12} F_B I G \Phi t_{det} V \frac{\Omega}{4\pi}\eta\right)} = C_1 \frac{S_f}{N_T F_B} = C_2 \frac{T S_f}{F_B} \tag{1}$$

where $\chi, S_f, s, N_T, B_{12}, F_B, I, G, \Phi, t_{det}, V, \Omega,$ and η are the tracer species mole fraction, fluorescence, saturation parameter, total population of molecules per unit volume, Einstein B absorption coefficient, Boltzmann fraction, laser irradiance, spectral overlap integral, fluorescence yield, detection time of the detector, volume probed by laser, detection solid angle, and the detector efficiency. The ratio in Equation 1 eliminates many of the parameters ($B_{12}, t_{det}, V, \Omega,$ and η) that are insensitive to position in the flow. Since the pressure in the boundary layer is low (230 Pa), the rate of collisional quenching of NO is assumed to be small. The maximum variation in the fluorescence yield through the boundary layer was computed to be 15%. Although the overlap integral has a temperature and pressure dependence, the laser frequency is centered on the J″=0.5 transition pair, making the term relatively insensitive to changes in the vertical direction. Calculations of the spectral integral *G* using CFD variable profiles has shown less than a 5% variation in *G* over the boundary layer thickness. Both the effects of saturation and absorption are also assumed to be negligible, thus eliminating *s* and *I*. As a result, χ_{rel} can be computed by using a normalizing constant, $C_1 = \left({F_B N_T}/{S_f}\right)_{\mathrm{wall}}$, which corresponds to the wall value computed at each x position. Using the ideal gas law, and assuming a zero pressure gradient in the wall-normal direction, Equation 1 can be further simplified using a new normalizing constant, $C_2 = \left({F_B}/{T S_f}\right)_{\mathrm{wall}}$, which only requires the temperature, *T*, and the fluorescence, S_f, at the wall since F_B is only a function of *T*. For this analysis the J″=0.5 transition pair was chosen due to its relatively low temperature sensitivity compared to the other transitions. This minimizes error propagated into the mole fraction measurement from the previous PLIF thermometry results. Figure 3 illustrates the relative mole fraction measurement computed from Eq. 1, compared to CFD mole fraction, which has also been normalized to its surface value.

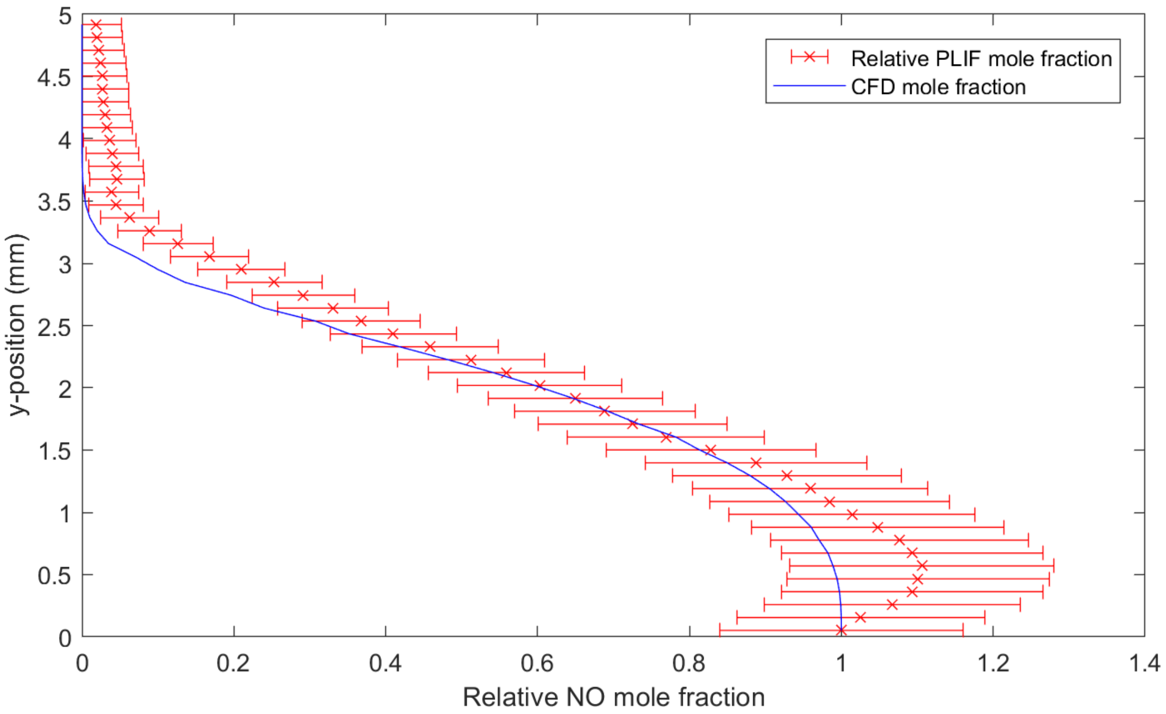

Fig. 3 Relative mole fraction measurement compared with CFD results (x = *85mm*)

The absolute mole fraction measurement relies on incorporating the relative mole fraction profile with a scaling constant derived from conservation of mass:

$$\dot{m}_{NO} = \int_0^\delta \varrho_{NO}\boldsymbol{u}\, dy = constant \tag{2}$$

where $\dot{m}_{NO}$ is the NO mass flow rate ejected through the seeding slot, ϱ_{NO} is the NO species density, u is the streamwise velocity, and δ is the boundary layer thickness. This equation can be expressed as the following:

$$\dot{m}_{NO} = \int_0^\delta \frac{W\,\chi_{rel}\,P\,M_{NO}}{R_u\,T}\boldsymbol{u}\, dy = constant \tag{3}$$

where M_{NO} is the molar mass of NO, N_{NO} is the number density of NO, and R_u is the universal gas constant. A scaling factor, *W*, multiplied by the relative mole fraction profile, χ_{rel}, is introduced to replace the absolute mole fraction, χ_{NO}. Equation 3 is then re-arranged for the scaling constant, *W*:

$$W = \frac{\dot{m}_{NO}\,R_u}{M_{NO}\,P\int_0^\delta \frac{\chi_{rel}\boldsymbol{u}}{T}\, dy} \tag{4}$$

The absolute mole fraction is obtained by multiplying the relative mole fraction profile by *W*:

$$\chi_{NO} = W\chi_{rel} \tag{5}$$

The velocity can be provided by either experimental or numerical data, or an assumed similarity profile. Note that prior MTV experimental data performed on the same experimental setup is used in the present work [23]. While the wall-normal pressure gradient was assumed to be negligible, the viscous interaction that occurs at the leading edge leads to a stream-wise pressure gradient [32]. However, the imaging region is in the "weak viscous interaction" region of the boundary layer, resulting in a negligible stream-wise pressure profile [33]. Therefore the pressure was assumed to be a constant 230 Pa in the boundary layer, measured with a pressure tap in the experiment. Temperature is provided using NO-PLIF thermometry reported in the literature from the same experimental data set [17].

In the experiment, the mass flow rate of NO was controlled by a mass-flow controller (MFC) located between the NO supply bottle and the wedge model. In situations where the mass flow rate is not known, the scaling constant, *W*, can be computed with an alternate method. This method involves integrating Equation 3 for two separate x-positions, and imposing conservation of mass on the flow of both air and NO in the boundary. This results in Equations 6 and 7, which form a simple system of equations that can be solved for W_1 and W_2. These variables represent the scaling constants for x-positions 1 and 2.

$$\int_0^{\delta_v} \frac{W_1 \chi_{rel,1}\, P_1}{T_1} \boldsymbol{u_1}\, dy = \int_0^{\delta_v} \frac{W_2\, \chi_{rel,2}\, P_2}{T_2} \boldsymbol{u_2}\, dy \tag{6}$$

$$\int_0^{\delta_v} \frac{(1 - W_1 \chi_{rel,1}\,) P_1}{T_1} \boldsymbol{u_1}\, dy = \int_0^{\delta_v} \frac{(1 - W_2\, \chi_{rel,2}\,) P_2}{T_2} \boldsymbol{u_2}\, dy \tag{7}$$

The mole fraction measurements reported in the current work were calculated using an NO mass flow rate measured by the MFC. The absolute mole fraction map is compared to CFD mole fraction results in Figure 4. Mole fraction profiles are compared to CFD in Figure 5 for 3 different x-positions (x=60, 85, and 110 mm). The error bars in the figure include uncertainty in determining the edge of the concentration boundary layer and the error propagated from the NO-PLIF thermometry data [17].

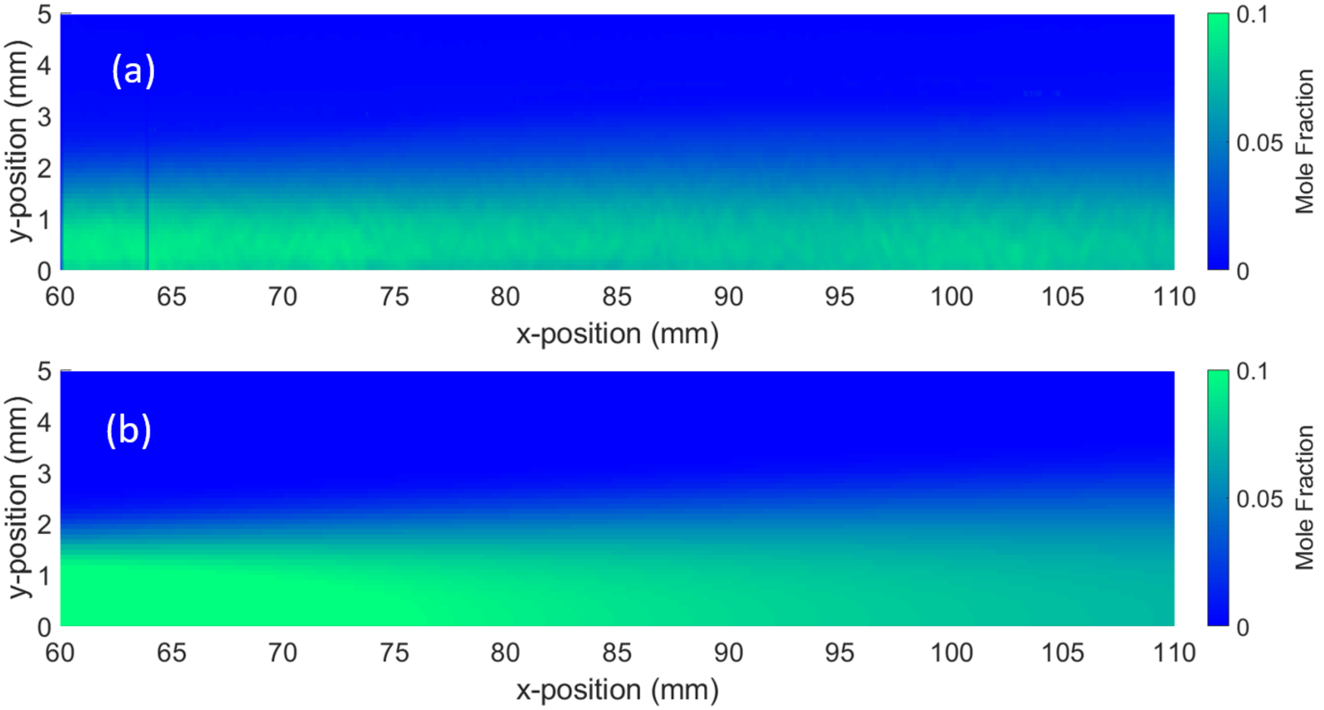

Fig 4. NO mole fraction measurement (a) compared with CFD results (b)

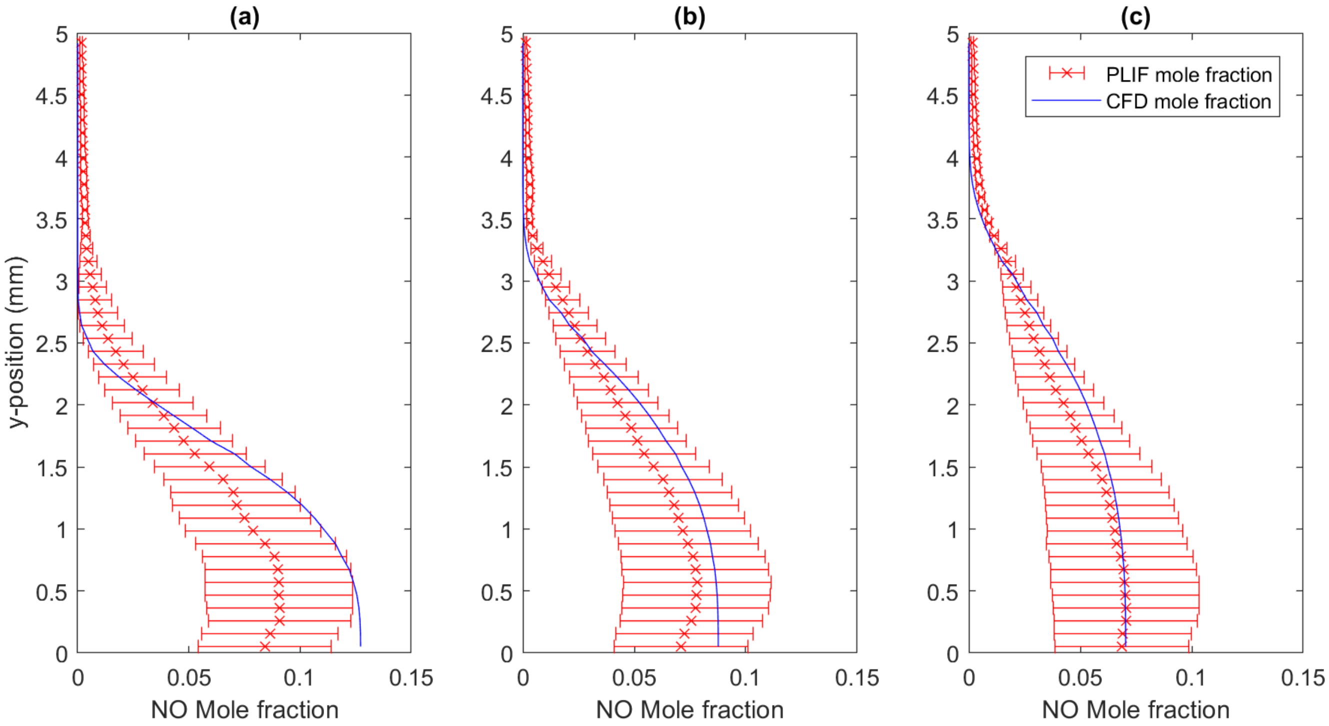

Fig 5. NO mole fraction profiles compared with CFD results at (a) x=60 mm, (b) x=85 mm, and (c) x=110 mm

The mole fraction measurement deviated from the mole fraction predicted by CFD by an average of 5.8%. The maximum deviation between the CFD and PLIF predicted mole fractions was approximately 18%. The mole fraction measurement showed better agreement with CFD further downstream. The most likely cause of this discrepancy is inaccuracies during integration of the boundary layer, as the temperature profile is less accurate upstream [17]. It is not clear why the wall-normal mole fraction gradient at the wall is non-zero. Error in the temperature predictions, or a combination of absorption and saturation effects [17], which were assumed to be negligible in the current work, could have contributed to the discrepancy.

3.2 Heat Flux Measurement

Wall heat flux (q_y) can be calculated by using the mole fraction and temperature results obtained in the previous sections. Integration of the conservation of energy equation in the boundary layer yields the following relation:

$$\int_0^y \rho \boldsymbol{u} \frac{\partial}{\partial x}\left(h + \frac{|\vec{V}|^2}{2}\right) dy + \int_0^y \rho \boldsymbol{v} \frac{\partial}{\partial y}\left(h + \frac{|\vec{V}|^2}{2}\right) dy = -\left[q_y\right]_0^y + [\tau \boldsymbol{u}]_0^y \qquad (8)$$

where q_y is solved from this relation by integrating two boundary layer profiles of velocity and temperature at a short distance apart (dx = 0.104 mm in this work). There are two principal methods by which this can be done. If complete and high-quality temperature and velocity boundary layer profiles are available, then the integration can be performed over the entire boundary layer (from 0 to δ_v). In this case, it is known that at $y = \delta_v$, $q_{y,\delta} = 0$ and $\tau u_\delta = 0$ and at $y = 0$, $\tau u_0 = 0$. Therefore, the above equation can be manipulated to give:

$$q_{y,0} = \int_0^{\delta_v} \rho \boldsymbol{u} \frac{\partial}{\partial x}\left(h + \frac{|\vec{V}|^2}{2}\right) dy + \int_0^{\delta_v} \rho \boldsymbol{v} \frac{\partial}{\partial y}\left(h + \frac{|\vec{V}|^2}{2}\right) dy \tag{9}$$

When accurate temperature and velocity profiles are not available out to the edge of the boundary layer, the heat flux can still be solved by integrating to the temperature maxima of the boundary layer profiles. In this case, since at $y = y_{Tmax}$, $q_{y,y_{Tmax}} = 0$ and $\tau \boldsymbol{u}_{y_{Tmax}} = \boldsymbol{u}\mu \frac{\partial \boldsymbol{u}}{\partial y}$, Equation 9 becomes:

$$q_{y,0} = \int_0^{y_{T_{max}}} \rho \boldsymbol{u} \frac{\partial}{\partial x}\left(h + \frac{|\vec{V}|^2}{2}\right) dy + \int_0^{y_{T_{max}}} \rho \boldsymbol{v} \frac{\partial}{\partial y}\left(h + \frac{|\vec{V}|^2}{2}\right) dy - \mu \boldsymbol{u}_{y_{T_{max}}} \frac{\partial \boldsymbol{u}}{\partial y} \tag{10}$$

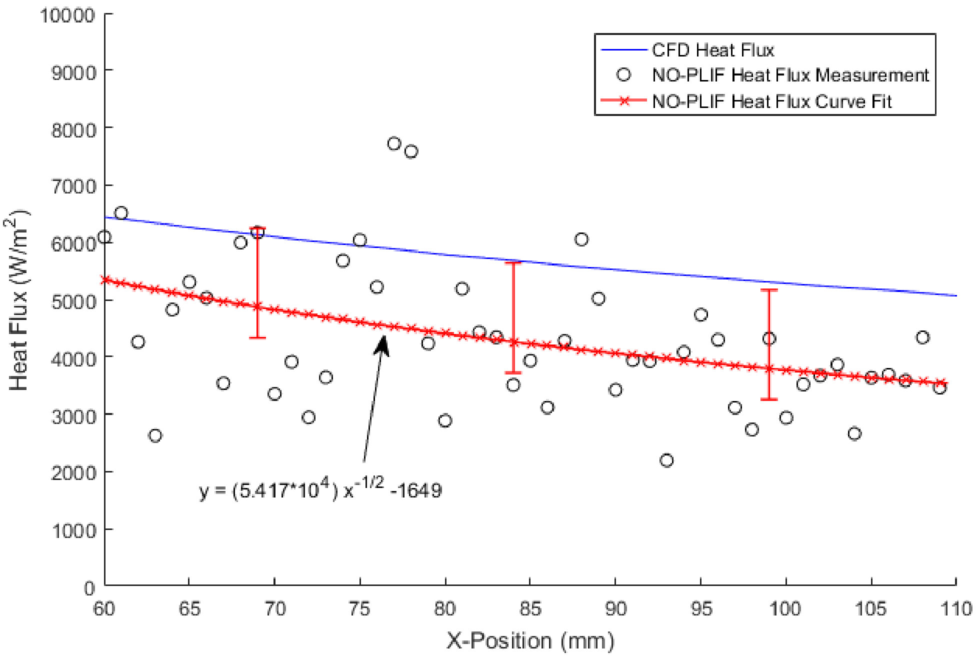

Fig 6. NO-PLIF surface heat flux compared to CFD values

A velocity profile must be known to calculate the wall heat flux $q_{y,0}$with the above equations. This can be achieved through an accompanying velocimetry measurement such as MTV, or with an approximation such as the Blasius similarity profile.

Wall heat flux was calculated in the present work using Equation 10 (as the experimental temperature data did not extend all the way to the edge of the boundary layer) and MTV velocity data. The results are shown in Figure 6 and are compared to heat flux predicted by CFD.

The heat flux measurement was determined to be 26.8% lower than the CFD heat flux on average. This difference is attributed to neglecting enthalpy flux in the y-direction. The error bars shown in the figure are based on an analysis of this enthalpy flux from the CFD. The additional error in both directions is the standard error associated with the scatter of data points. The lack of a wall-normal velocity measurement is a limitation of using an MTV velocity profile, which contains only x-direction velocity information [23]. An additional error is the uncertainty in CFD heat flux calculations from the imposed boundary condition. The plate temperature boundary condition was set at 314 K, which was measured from a thermocouple placed on the inner hollow surface of the wedge [17]. This error is currently not quantifiable, and does not contribute to the error bars in Figure 6.

3.3 Near-Surface Temperature Correction

The heat flux measurement determined in Section 3.2 can be used to correct near-wall temperature measurements that were previously published [17]. The near-surface temperature is difficult to obtain in tracer-seeded PLIF experiments due to camera resolution issues combined with absorption and saturation effects. Other studies have also had difficulty measuring near-surface temperatures using PLIF thermometry [18]. The temperature is corrected by estimating a heat flux and then using Fourier's Law, shown below.

$$Q = -k\frac{dT}{dy} \tag{14}$$

where k is the thermal conductivity of the fluid mixture. This equation is rearranged to solve for the temperature gradient from the heat flux. The temperature measurement from this experiment was corrected in the linear regime near the surface. The linear region was approximated as the distance halfway to the peak temperature in the boundary layer. For x=85 mm this distance was approximately 0.46 mm off the surface. The heat flux at x=85 mm was calculated to be 4227 W/m^2, which was measured from the curve fit on Figure 6. Figure 7 shows the temperature correction using Fourier's law at x=85 mm. The correction was applied to the best-performing thermometry method in a previous work, spectral peak method (SPM) thermometry. The reader is directed to McDougall *et. al.* [17] for more information regarding this technique. As shown in the figure, near-wall temperature measurements are corrected by approximately 30-35 K, bringing them closer to the CFD.

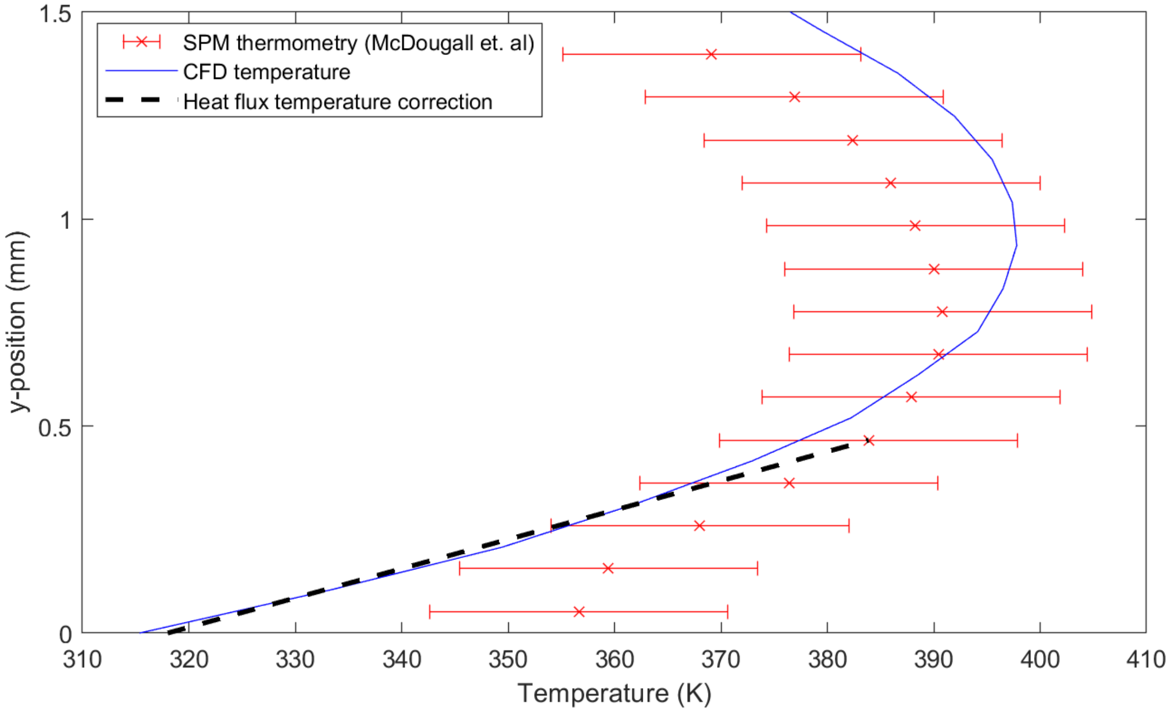

Fig 7. Near-surface temperature correction using heat flux measurement

4. Conclusions

This study outlines a detailed method of obtaining multiple primitive and derived flow properties in a hypersonic boundary layer from NO-PLIF imaging. Absolute NO mole fraction was determined, on average, within 5.8% of CFD simulated results. The heat flux measurement followed the same general trend as the CFD simulated curves. This measurement was on average 26.8% lower than CFD simulated values, and was probably due to the absence of vertical velocity components in the MTV data set. Heat transfer measurements were used to partially correct the temperature predictions from a previous study [17]. The surface temperatures were shifted approximately 30-35 K lower than the previous PLIF thermometry predictions. These corrections lowered all measured temperatures near the wall, showing better agreement with the CFD predictions. This temperature correction can be applied to any flat plate laminar boundary layer for which the heat flux is known to correct for camera resolution problems, absorption and saturation effects.

References

1. Asano, K. *Mass Transfer: From Fundementals to Modern Industrial Applications*: Wiley, 2006.
2. Hinman, W. S., and Johansen, C. T. "Rapid prediction of hypersonic blunt body flows for parametric design studies," *Aerospace Science and Technology* Vol. 58, 2016, pp. 48-59.
3. Merchant, V., and Radhakrishnan, J. "Design and optimization of a supersonic intake," *Conference series on Materials and Engineering*. 2017.
4. Casper, K. M., Beresh, S. J., Henfling, F. F., Spillers, W. W., Pruett, B., and Schneider, S. P. "Hypersonic wind-tunnel measurements of boundary-layer pressure fluctuations," *39th AIAA Fluid Dynamics Conference*. San Antonio, 2009.
5. Schneider, S. P. "Effects of roughness on hypersonic boundary-layer transition," *Journal of Spacecraft and Rockets* Vol. 45, No. 2, 2008, pp. 193-209.
6. George, W. K. "Recent advancements toward the understanding of turbulent boundary layers," *4th AIAA Theoretical Fluid Mechanics Meeting*. Toronto, 2005.
7. Roy, C., and Blottner, F. "Review and asessment of turbulence models for hypersonic flows," *Progress in Aerospace Science* Vol. 42, 2006, pp. 469-530.
8. Splinter, S. C., Bey, K. S., Gragg, J. G., and Brewer, A. "Comparative measurements of earth and martian entry envionments in the NASA Langley HYMETS facility," *49th AIAA Aerospace Sciences Meeting*. Orlando, 2011.
9. Bonnet, J., Gresillon, D., and Taran, J. "Nonintrusive measurements for high-speed, supersonic and hypersonic flows," *Annu. Rev. Fluid Mech.* Vol. 30, 1998, pp. 231-273.
10. Boutier, A. "New Trends in Instrumentation for Hypersonic Research," *NATO ASI*. Vol. 224, 1993.
11. Ivey, C. B., Danehy, P. M., Bathel, B. F., Dyakonov, A., Inman, J., and Jones, S. B. "Comparison of PLIF and CFD results for the Orion CEV RCS jets," *49th AIAA Aerospace Sciences Meeting*. Orlando, 2011, pp. 1-21.
12. Johansen, C. T., Danehy, P. M., Ashcraft, S., Bathel, B. F., Inman, J. A., and Jones, S. B. "PLIF study of mars science laboratory capsule reaction control system jets," *41st AIAA Fluid Dynamics Conference and Exhibit*. 2011.
13. Palma, P. "Laser induced fluorescence imaging in free piston shock tunnels." Australian National University, 1999.
14. Eckbreth, A. C. "Recent advances in laser diagnostics for temperature and species concentration in combustion," *18th Symposium (International) on Combustion*. Vol. 18, Waterloo, 1981, pp. 1471-1488.
15. Danehy, P. M., Bathel, B. F., Johansen, C. T., Winter, M., Cutler, A. D., and O'Byrne, S. "Molecular-based optical measurement techniques for nonequilibrium hypersonic flows," *Hypersonic Nonequilibrium Flows: Fundementals and Recent Advances*. 2015.
16. Inman, J. A., Bathel, B. F., Danehy, P. M., Jones, S. B., Gragg, J. G., and Splinter, S. C. "Nitric oxide planar laser-induced fluorescence measurements in the hypersonic materials environmental test system," *AIAA Journal* Vol. 51, 2013, pp. 461-472.
17. McDougall, C. C., Hinman, W. S., Johansen, C. T., Bathel, B. F., Inman, J. A., and Danehy, P. M. "Nitric oxide planar laser-induced fluorescence thermometry measurements in a hypersonic boundary layer," *AIAA Propulsion and Energy Forum*. Atlanta, 2018.
18. Yoo, J. "Strategies for planar laser-induced fluorescence thermometry in shock tube flows." Stanford, 2011.

19. Fox, J. S., Danehy, P. M., and Houwing, A. F. P. "Instantaneous PLIF measurement of species mole-fraction in a varying temperature supersonic flow," *21st international Council of Aeronautical Sciences (ICAS) Congress*. Melbourne, 1998.
20. Heinze, J., Meier, U., Behrentdt, T., Willert, C., Geigle, K. P., Lammel, O., and Luckerath, R. "PLIF thermometry-based on measurements of absolute concentrations of the OH radical," *Physical Chemistry* Vol. 225, 2011, pp. 1341-1351.
21. Donohue, J. M., and McDaniel, J. C. "Computer-controlled multiparameter flowfield measurements using planar laser-induced iodine fluorescence," *AIAA Journal* Vol. 34, No. 8, 1996, pp. 1604-1611.
22. Hiller, B., and Hanson, R. K. "Simultaneous planar measurements of velocity and pressure fields in gas flows using laser-induced fluorescence," *Applied Optics* Vol. 27, No. 1, 1988, pp. 33-48.
23. Bathel, B. F., Danehy, P. M., Inman, J. A., Jones, S. B., Ivey, C. B., and Goyne, C. "Velocity profile measurements in hypersonic flows using sequentially imaged fluorescence-based molecular tagging," *AIAA Journal* Vol. 49, No. 9, 2010, pp. 1883-1896.
24. Battles, B. E., and Hanson, R. K. "Laser-induced fluorescence measurements of NO and OH mole fraction in fuel-lean high-pressure (1-10atm) methane flames: fluorescence modeling and experimental validation," *J. Quant. Spectrosc Radiat. Transfer* Vol. 54, 1995, pp. 521-537.
25. Thurber, M. C., and Hanson, R. K. "Simulataneous imaging of temperature and mole fraction using acetone planar laser-induced fluorescence," *Experiments in Fluids* Vol. 30, 2001, pp. 93-101.
26. Shi, L., Mao, X., and Jaworkski, A. J. "Application of planar laser-induced fluorescence measurement techniques to study the heat transfer characteristics of parallel plate heat exchangers in thermoacoustics devices.," *Measurement Science & Technology* Vol. 21, 2010.
27. Sanchez-Gonzalez, R., Bowersox, R. D. W., and North, S. W. "Simultaneous velocity and temperature measurements in geaseous flowfields using the vibrationally excited nitric oxide monitoring tecdhnique: a comprehensive study," *Applied Optics* Vol. 51, No. 9, 2012, pp. 1216-1228.
28. Bessler, W. G., Schultz, C., Lee, T., Jeffries, J. B., and Hanson, R. K. "Strategies for laser-induced fluorescence detection of nitric oxide in high-pressure flames. I. A-X(0,0) excitation.," *Applied Optics* Vol. 41, No. 18, 2002, pp. 3547-3557.
29. Reisel, J. R., Campbell, D. C., and Laurendeau, N. M. "Einstein coefficients for rotational lines of the (0,0) band of the NO A2Sigma(+)-X2Pi system," *J. Quant. Spectrosc. Radiat. Transfer* Vol. 47, No. 1, 1992, pp. 43-54.
30. Arisman, C. J., Johansen, C. T., Bathel, B. F., and Danehy, P. M. "Investigation of gas seeding for planar laser-induced fluorescence in hypersonic boundary layers," *AIAA Journal* Vol. 53, No. 12, 2015, pp. 3637-3651.
31. Arisman, C. J., and Johansen, C. T. "Nitric oxide chemistry effects in hypersonic boundary layers," *AIAA Journal* Vol. 12, 2014, pp. 1-64.
32. Luca, L. d., Cardone, G., Chevalerie, D. A. d. l., and Fonteneau, A. "Viscous interaction phenomena in hypersonic wedge flow," *AIAA Journal* Vol. 33, No. 12, 1995, pp. 2293-2298.
33. Anderson, J. D. *Hypersonic and High Temperature Gas Dynamics*: McGraw-Hill, 2006.